Fouling characteristics of microcrystalline cellulose during cross-flow microfiltration: Insights from fluid dynamic gauging and molecular

N.B. When citing this work, cite the original published paper.

(article starts on next page)

Fouling characteristics of microcrystalline cellulose during cross-flow microfiltration: Insights from fluid dynamic gauging and molecular dynamics simulations

Kenneth Arandia[1], Nabin Kumar Karna[1], Tuve Mattsson, Anette Larsson, Hans Theliander [*]

Department of Chemistry and Chemical Engineering, Chalmers University of Technology, SE 412 96, Gothenburg, Sweden
Wallenberg Wood Science Center, Chalmers University of Technology, SE 412 96, Gothenburg, Sweden

ABSTRACT

The fouling behaviour of microcrystalline cellulose (MCC) particles on polyethersulfone (PES) membranes was investigated using fluid dynamic gauging (FDG) and molecular dynamics (MD) simulations. Experimental cross-flow microfiltration (MF) of a dilute MCC suspension at 400 mbar transmembrane pressure using 0.45 μm PES membranes revealed an estimated fouling layer thickness of 616 ± 5 μm for both fouled and re-fouled membranes at an applied shear stress of 37 ± 2 Pa. A decline in pure water flux was observed after each membrane cleaning and flushing procedure, indicating that highly resilient layers were formed close to the membrane surface. A possible explanation for the formation of resilient cellulose layers was obtained through MD simulations of the free energy profiles, which predicted deep energy minima at close interparticle separations of the cellulose–cellulose and cellulose–PES systems. The consequence of this energy minima is that attractive and repulsive forces are in balance at a specific distance between the particles, suggesting high binding energy at close interparticle distances. This implies that a certain force is needed to remove the layer or redisperse the cellulose particles. MD simulations also suggested that contributions made by repulsive hydration forces negatively influenced the adsorption of cellulose particles onto the PES membrane. These results highlight how experimental FDG measurements, when complemented with MD simulations, can provide insights into the fouling behaviour of an organic model material during cross-flow filtration.

1. Introduction

Studies on the processing of lignocellulosic biomass for various biorefinery applications are gaining substantial interest in the transition of process industries from fossil-based to bio-based resources [1–3]. As an energy-efficient and highly selective operation, pressure-driven membrane processes can be expected to be employed in the pretreatment and downstream processing of lignocellulosic biomass [4] to produce renewable, value-added materials. Different applications of membrane processes in biorefineries has, however, proved to be challenging, primarily due to membrane fouling [5–7].

Fouling is the process by which suspended or dissolved substances are deposited on the surface, at the pore openings, or within the pores of a membrane [8] and results in a decline in the performance of membrane processes. It limits the production capacity by lowering the flux or changing the selectivity of the membrane over time [9]. There are two types of fouling based on the interaction of foulants with the membrane material: reversible and irreversible fouling. Reversible fouling, which occurs when foulants are loosely attached to the membrane surface, results in the formation of a dynamic cake or gel layer. This layer can be removed effectively by physical cleaning. Irreversible fouling, in direct contrast, occurs when foulants are tightly bound to the membrane due to adsorption or pore blocking and requires the use of chemical cleaning agents to restore the flux or membrane selectivity. In filtration systems where the feed material contains complex macromolecules, dissolved components, and suspended particles, fouling is practically inevitable, especially when the components have a high affinity towards the membrane material, are near their solubility limit, or are in a metastable concentration range. Complex filtration systems require an in-depth understanding of fouling mechanisms in order to devise appropriate fouling strategies.

It is customary to identify the severity of fouling by a decline in flux or an increase in transmembrane pressure (TMP), but these do not provide reliable measures of the properties of the fouling layer and the type of membrane fouling. Advanced studies on membrane fouling

---

have made significant progress in monitoring of the fouling behaviour [10,11], along with the development of analytical techniques to characterize fouled membranes [12–14]. Nevertheless, despite the advances in fouling monitoring and membrane characterization, studies that focus on the mechanistic understanding of membrane fouling remain limited: membrane fouling behaviour is still difficult to predict and model. Mechanistic models for determining the fouling rate during cross-flow filtration, which include the critical flux model [15], shear-induced diffusivity [16], inertial lift [17], and particle capture [18] have been reported. These models are nevertheless difficult to apply directly to complex fouling systems in which interparticle interactions are present. Advanced techniques for monitoring fouling layer development are therefore necessary to provide hydrodynamic information of the fouling layers formed.

Numerous *in situ* monitoring techniques have been developed over the years to investigate the formation of fouling layers. These include direct observation [19], laser-based techniques [20], ultrasonic time-domain reflectometry [21], nuclear magnetic resonance imaging [22], confocal laser scanning microscopy [23], small angle scattering [24], electrical impedance spectroscopy [25], and fluid dynamic gauging (FDG) [26,27]. Among these techniques for fouling investigation, FDG offers unique information not available with other techniques. It is an *in situ*, real-time monitoring technique that provides an indication of the thickness of the fouling layers formed and their local strength properties at different positions. FDG is relatively inexpensive, requires minimal sample preparation, and is applicable for different types of fluids. Tuladhar *et al.* [26] first developed this technique for local thickness measurements of soft deposits on solid surfaces. It was expanded further to membrane filtration of model materials such as ballotini suspensions [28–30], yeast suspensions [31], synthetic microparticles [32], and Kraft lignin [33–35]. Previous studies have also investigated the fouling characteristics of microcrystalline cellulose (MCC) and used FDG to determine the influence of pH and cross-flow velocity (CFV) on the thickness and strength of fouling layers formed on polymeric membranes [36,37].

Although *in situ* monitoring techniques can provide relevant information regarding the development of fouling layers, the experimental techniques currently available cannot provide information at the molecular level, which is crucial for an increased mechanistic understanding. Less attention has been given to investigating the fouling mechanisms, and the mechanistic understanding of the fouling phenomena remains to be explored further. Molecular dynamics (MD) has been used to obtain information on different systems involving membrane filtration. For example, in a study of pore wetting, Tanis-Kanbur *et al.* used MD simulations [38] to show that the surfactant-salt affinity increased at higher salt concentrations. Similarly, Meconi *et al.* [39] studied the adsorption and desorption behaviour of surfactants onto a membrane surface and elaborated on the relationship between the attractive force and concentration. Shi *et al.* [40] used experiments and complemented their results with MD simulations to investigate the formation of a compact and continuous hydration layer on a zwitterionic membrane which played a crucial role in membrane filtration. Similarly, using both experimental techniques and MD simulations, Ma *et al.* [41] showed that local interactions were critical during lysozyme fouling on a polyvinylidene fluoride membrane under different filtration conditions. Thus, MD simulations can be performed as a tool to reveal information on the fouling mechanisms that occur at the molecular level [42]. In this context, MD and experimental methods can act as complementary tools [38,40], where MD can be used to unveil nanoscale effects at the membrane-solvent interface.

In this study, the fouling behaviour of a dilute MCC suspension was investigated during cross-flow microfiltration (MF) at 400 mbar TMP using 0.45 μm polyethersulfone (PES) membranes. In addition, a series of membrane flushing and physical cleaning in between the FDG measurements was performed, which has not been done in previous
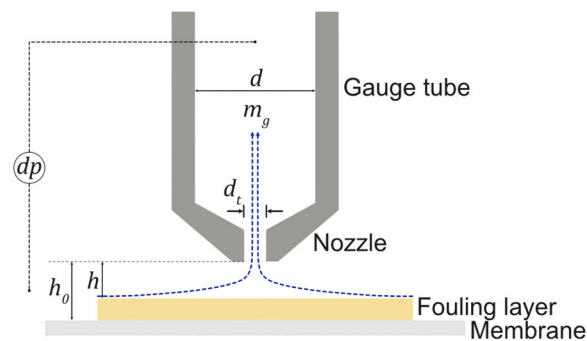

Fig. 1. Schematic diagram of the FDG probe over a fouled membrane surface. The probe consists of a gauge tube with a tapered nozzle, where d is the inner diameter of the gauge tube ($d = 3$ mm) and d_t is the inner diameter of the nozzle orifice ($d_t = 0.5$ mm). m_g is the gauging mass flow rate, dp is the pressure drop over the probe, h_0 is the gauge height above the membrane, and h is the gauge height above the fouling layer.

FDG studies on MCC particles. In parallel with the cross-flow MF experiments, MD simulations have been employed in the present study to investigate the formation of resilient fouling layers on polymeric membranes during cross-flow MCC filtration. Although MD simulations have been used to study the fouling mechanisms on different membranes [42–44], the present study extends further to estimate the enthalpic and entropic contributions to the free energy during the fouling of the PES membrane with cellulose particles. The primary focus is on the mechanistic investigation of the foulant–foulant and foulant–membrane interactions at the interface by calculating the free energy profiles. This work attempts to highlight how the combination of FDG and MD simulations can provide insights into the fouling characteristics of an organic model material during cross-flow MF.

2. Experimental

2.1. Fluid dynamic gauging (FDG)

FDG follows the principles of fluid mechanics whereby a pressure drop is generated due to flow constriction between the tip of a nozzle and the surface of a fouling layer, as illustrated in Fig. 1. The applied differential pressure is correlated to the distance from the surface of the FDG probe at a known membrane position as the probe approaches the fouling layer.

The thickness of the fouling layer, δ, is given by Eq. (1) [26]:

$$\delta = h_0 - h \tag{1}$$

where h_0 is the gauge height above the membrane and h is the gauge height above the fouling layer.

The cohesive or adhesive strength of fouling layers can also be estimated using FDG concurrent with the thickness measurements. Fluid shear stress is exerted on the surface of a fouling layer as the probe is moved closer to the surface, resulting in the removal of loose fouling layers. It is possible to track the shear-induced removal of fouling layers at elevated fluid shear. The maximum shear stress, $\tau_{w,max}$, can be calculated analytically using Eq. (2), with the assumption of a creeping concentric flow between parallel plates [33]:

$$\tau_{w,max} = \frac{6\mu m_g}{\pi \rho h^2} \cdot \frac{1}{d_t} \tag{2}$$

where μ is the dynamic viscosity of the fluid, m_g is the gauging mass flow rate, ρ is the density of the fluid, h is the gauge height above the fouling layer, and d_t is the inner diameter of the nozzle orifice. $\tau_{w,max}$ is in the region directly underneath the inner edge of the nozzle rim at a radial distance $d_t/2$ from the central axis of the gauge tube. The calculation of $\tau_{w,max}$ in Eq. (2) is simplified as only h varies while
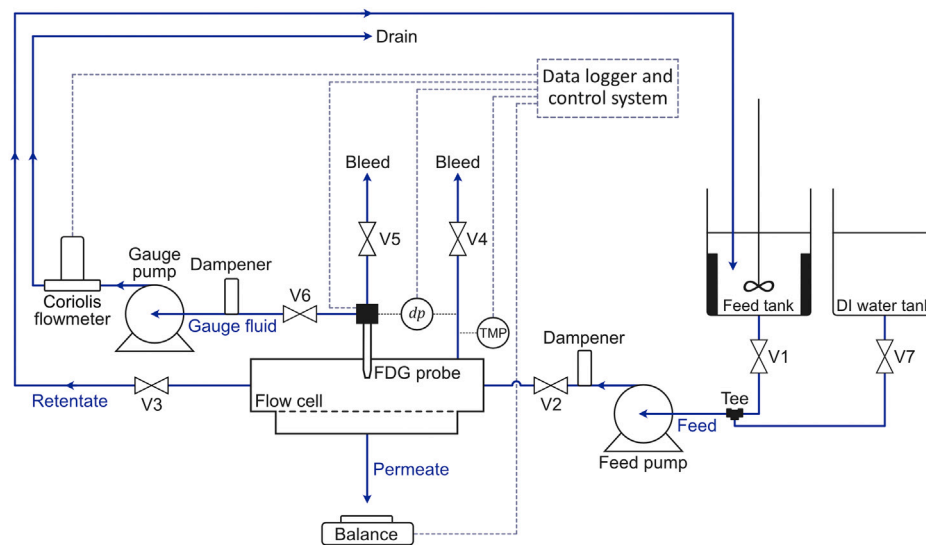
Fig. 2. Schematic diagram of the cross-flow filtration test rig showing the different process streams: feed, permeate, retentate and gauge fluid.

other terms are kept constant during the FDG measurements. The $\tau_{w,max}$ value provides an estimate of the fluid shear stress required to remove individual cake layers and thus indicates the local cohesive or adhesive strength of the cake.

2.2. Membrane and cake resistance

Employing Darcy's Law, the membrane resistance in a pure solvent system, R_m, can be calculated using Eq. (3) thus:

$$R_m = \frac{TMP}{J\mu} \tag{3}$$

where J is the flux and μ is the dynamic viscosity of the fluid.

When filtering a solution or a suspension, the resistance-in-series model (Eq. (4)) can be used to include reversible and irreversible fouling:

$$J = \frac{TMP - \Pi}{\mu R_T} = \frac{TMP - \Pi}{\mu(R_m + R_{rev} + R_{irrev})} \tag{4}$$

where Π is the osmotic pressure, R_T is the total resistance, R_{rev} is the reversible fouling resistance, and R_{irrev} is the irreversible fouling resistance.

The cake resistance, R_c, can be determined by rearranging Eq. (4) and excluding the contributions from Π and pore fouling:

$$R_c = \frac{TMP}{J\mu} - R_m \tag{5}$$

2.3. Cross-flow filtration rig

All cross-flow MF experiments were performed using the bench-scale, stainless steel filtration test rig equipped with a flow cell and an FDG probe shown in Fig. 2. The test rig was operated in a *feed-and-bleed* configuration whereby the retentate is recycled back to the inlet of the feed tank. The technical specifications of each component are described in detail in previous studies [36,45]. The PES membrane was mounted at the bottom of the cross-flow channel of the flow cell after being soaked in deionized water at least half an hour prior to MF. Two supporting layers, a porous polypropylene sheet and a perforated stainless steel slab with holes 2 mm in diameter, were placed underneath the membrane to secure its position. The polypropylene sheet was placed on top of the stainless steel slab.

The inlet section of the test rig was equipped with a three-way tee union, a 12 mm ball valve (V7), and a separate tank for deionized water to simplify the feed change from deionized water to MCC suspension

and also to prevent air bubbles from entering into the system. All logged data was monitored via LabVIEW™ 2020 (National Instruments), with a detailed description of its automation reported by Lewis [46].

2.4. Materials

Flat, hydrophilic PES membranes (Supor®, Pall Corporation), with a nominal pore size of 0.45 μm, were cut to dimensions of 200 mm × 30 mm to fit into a rectangular cross-flow filtration cell with an active membrane surface area of 2.4×10^{-3} m^2 (150 mm × 16 mm), as in the procedures carried out by Zhou *et al.* [36]. The manufacturer of the membrane specified the pure water flux of the PES membranes to be 3.5×10^4 L m^{-2} h^{-1} at 0.7 bar TMP.

Commercially available MCC (Avicel® PH-105, DuPont Nutrition), with a nominal particle size of 20 μm, was selected as the model material for all cross-flow MF experiments. Prior to each MF experiment, a suspension was prepared from 9.8 g of MCC in 4 L deionized water to obtain a solids content of 0.15 vol%. The specific surface area and solid density of MCC are 2.1 m^2 g^{-1} and 1560 kg m^{-3}, respectively [47]. The suspension was homogenized using an IKA Ultra-Turrax® T50 with an S50 N-G45F dispersing element at a rotational speed of 10000 rpm for 15 min. After the mechanical pretreatment, the suspension was placed in a 5 L baffled feed tank at an unadjusted pH of 6.2 and ambient temperature of 22-23 °C under constant stirring, using a pitched two-blade impeller, for a minimum of 12 h to ensure consistent swelling of the particles. The suspension was diluted further to a concentration of 0.02 vol% to prepare four 5 L suspensions for each sequence of cross-flow MF.

2.5. Filtration experiments

Each cross-flow MF sequence was comprised of four cycles of the following steps using the same PES membrane: determining the pure water flux and membrane position, MCC fouling, FDG measurements, and membrane cleaning and flushing. The fouled PES membrane was collected for SEM analysis at the end of each sequence.

All MF experiments were conducted with an initial MCC suspension volume of 5 L fed at a CFV of ∼0.07 m s^{-1}, which corresponds to a duct flow Reynolds number, $Re_{duct} = \sim 1200$, in the laminar regime. The TMP was kept at 400 ± 20 mbar, with larger variations during the feed change from deionized water to MCC suspension. The mass of the permeate was logged every two seconds to calculate the permeate flux, while m_g was kept constant at 0.1 g s^{-1} during FDG measurements (pressure-mode FDG).

2.5.1. Pure water flux and membrane position

The pure water flux was determined by circulating 5 L of deionized water for at least 2000 s (33.3 min). The exact position of the PES membrane was verified by noting the dp and h_0/d_t values and adjusting them with the h_0 offset value, $h_{0,\text{offset}}$, to overlap with the master calibration curve. The $h_{0,\text{offset}}$ value varies for each MF experiment and is used to correct the shift in the membrane's position. The adjusted membrane position can be determined by subtracting the $h_{0,\text{offset}}$ value from each measured h_0 so that it would superimpose with the calibration curve. Detailed procedures for the FDG calibration can be found in the Supplementary Material S1.

2.5.2. MCC fouling and FDG measurements

After verifying the position of the membrane, the FDG probe was retracted to the top of the flow cell to minimize its disturbance on the formation of the fouling layer. The feed line was then diverted from deionized water to the 0.02 vol% MCC suspension for at least 3000 s (50 min). Furthermore, the gauge flow was turned off to conserve the MCC suspension whilst no FDG measurements were conducted, since the gauge fluid was not recycled back into the system.

After an initial 3000 s (50 min) of fouling, the gauging fluid flow was turned on and withdrawn at a constant mass flow rate: $m_g = 0.1$ g s^{-1}. FDG measurements were conducted by moving the probe in small increments to approach the fouling layer being formed whilst the system was still subjected to cross-flow MF of the MCC suspension. The probe made a small imprint of ~1 mm in diameter, making its influence on the permeate flux curves negligible. The dp and h/d_t values are noted, and the measurements were terminated when dp exceeded 100 mbar. This dp is set to prevent the FDG probe from damaging the flat sheet PES membrane.

From the master calibration curve equation (Eq. S1), h_0/d_t can be calculated at the measured dp values ($h = h_0$, if no deposit is present). Using the calculated h_0/d_t value and the measured h/d_t value, the height of the fouling layer is determined by subtracting these two values at a dp that is in the incremental zone ($h_0/d_t \leq 0.25$).

2.5.3. Cleaning and flushing of the membrane

The probe was retracted after the first measurements were made and the membrane was dismounted from the flow cell to allow for visual inspection of the extent of fouling. Physical cleaning of the membrane was then undertaken by flushing the fouling layer with deionized water and removing it with a soft-bristled paintbrush, see also Supplementary Material S2. The test rig was also cleaned by circulating deionized water for 1800 s (30 min) to remove the remaining MCC.

The flow cell was mounted back together with the cleaned membrane and a fresh set of 5 L deionized water was circulated for at least 2000 s (33.3 min) to determine the new pure water flux and membrane position. The cross-flow MF sequence was subsequently continued for 3000 s (50 min) of additional fouling to allow MCC particles to redeposit on the active membrane surface. New measurements were conducted thereafter, and the MF sequence continued until four cycles had elapsed.

3. Computational method

All MD simulations were performed using GROMACS2020 software [48], which has been used extensively to study the atomistic details of systems involving biomolecules [49–51] and polymers [52,53]. The equations of motion were integrated by a velocity verlet algorithm with a time step of 2 fs and a cut-off distance of 1.1 nm was applied to truncate van der Waals forces. The Smooth Particle Mesh Ewald (SPME) method [54] was applied to calculate the long-range electrostatic interactions. The temperature of the systems was controlled by a velocity rescaling thermostat [55]: a modified version of the Berendsen thermostat that has been shown to enforce the correct NVT ensemble. Periodic boundary conditions were applied in all directions throughout the simulations. Water molecules were described using the extended simple point-charge (SPC/E) [56] model due to its close agreement with experimental hydrogen bond dynamics. The bonds and angles of the water molecules were conserved by using the SETTLE [57] algorithm.

Apart from the atomic configurations of the initial system, it is also very important that a force field (FF) that best describes the interactions between the atoms in the simulation systems is chosen. All-atom optimized potentials for liquid simulations (OPLS-AA) [58] force fields were used to describe the cellulose and PES membrane: these were chosen because they have been shown to reproduce cellulose structures [59,60] and different polymer membranes [61,62] correctly.

Cellulose was modelled by a rectangular slab of crystalline cellulose, as shown in Fig. 3a. The starting structure of cellulose crystals was obtained from Nishiyama *et al.* [63], with each cellulose chain being eight anhydroglucose units long. The cellulose crystals possess two different types of surfaces, namely 110 and 200, and interactions between the 110–110, 110–200, and 200–200 planes are therefore considered [64].

A PES polymer chain was created by repeating 200 monomer units (Fig. 3b) using AVOGADRO software [65]. Previous studies by Ahn *et al.* [66] and Shi *et al.* [67] have shown that a polymer with 60 repeating units effectively represents the characteristics of the polymer. As in Ahn *et al.* [66], one end of the polymer chain was terminated with a hydrogen atom while the other end was closed with a phenyl group. The initial polymer chain was placed between two graphene sheets along the Y-axis enclosed in a periodic box of $5 \times 5 \times 20$ nm^3 and allowed to fold spontaneously. Subsequently, the graphene sheets were moved towards each other at a constant velocity of 0.01 nm ps^{-1} along the Y-axis in order to create a polymer with a density of 1.34 g cm^{-3}, similar to that reported experimentally (1.37 g cm^{-3} [68]). Then, the graphene sheet was removed from the system and several annealing cycles were performed to reproduce a "natural" folding of the chain so that an amorphous membrane would be created with a realistic surface roughness. In all of these processes, only the X-axis of the simulation box was allowed to vary; all remaining axes were kept constant (Fig. 3).

The magnitude of interparticle interaction was calculated using umbrella sampling (US) and the weighted histogram analysis method (WHAM) [69]. The latter is used to calculate the potential of mean force (PMF) along a reaction coordinate which, in this case, was the interparticle separation of the center of mass (COM). For US simulations involving a cellulose–PES membrane system in water, the PES membrane was placed in a computational box of $3.20 \times 4.68 \times 12.00$ nm^3 and the cellulose crystal was placed at a separation distance of 2.1 nm from the PES surface. The surface to surface separation of the particles was described to be the average distance between the sixth carbon (C6) atoms that are attached to the hydroxyl group of the cellulose nanocrystal (CNC) surface and surface sulphur (S) atoms of the PES membrane. The box was filled with the required number of water molecules, depending on the case in question. The system was then energy minimized and equilibrated at 300 K in an NVT ensemble for 6 ns. Subsequently, position restraints of 500 kJ mol^{-1} nm^{-2} were applied to the PES membrane to fix it in the desired position. The US was started by initially pulling the CNC towards the PES membrane at a constant velocity of 0.005 nm ps^{-1} with a force constant of 65 MJ mol^{-1} nm^{-1} of the added harmonic potential. The system configurations were stored at 0.05 nm intervals, which were used for the US. The sampling time of 6 ns was used for all configurations.

For US simulations involving cellulose–cellulose interactions, two cellulose crystals were placed in a simulation domain of size $5.10 \times 10.36 \times 3.19$ nm^3 at a certain interparticle separation. The simulation box was then filled with water molecules. After initial energy minimization and equilibration, one of the crystals was used as a reference and restrained in position while the other crystal was pulled towards it with a pulling force constant of 65 MJ mol^{-1} nm^{-1}. The remaining US procedure was similar to the one described above for the cellulose–PES membrane system. However, the mobile CNC, which is free to move along the direction of the reaction coordinate, is position restrained by
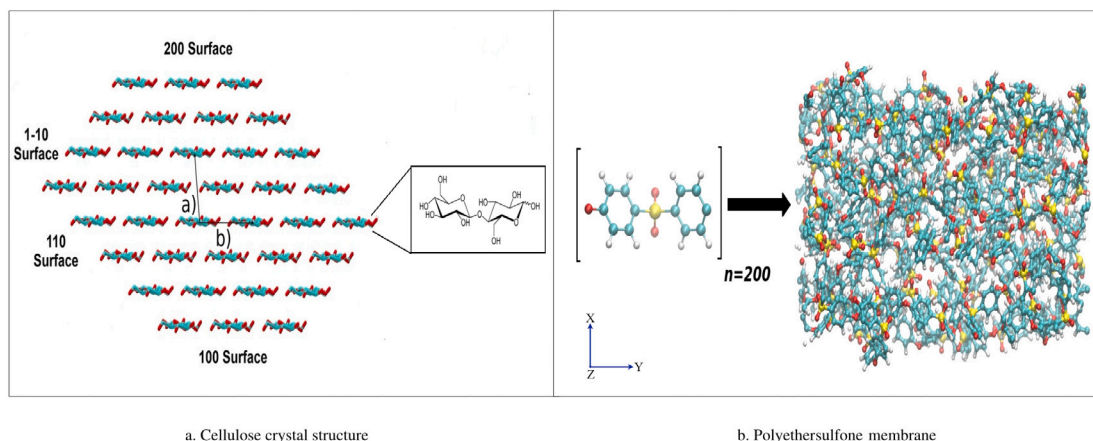
a. Cellulose crystal structure

b. Polyethersulfone membrane

Fig. 3. (a) A cellulose crystal and its respective faces and (b) the repeating unit of a PES molecule (within bracket) and a membrane formed from 200 PES units.

applying a force constant of 500 kJ mol^{-1} nm^{-2} on the carbon atoms along the remaining directions. This was done to prevent the rotation of the CNCs with respect to each other and ensure the relative surface orientation during the pulling process.

Entropy was calculated from the finite difference temperature derivative of PMF or ΔG at each interparticle separation (r) using Eq. (6) [70]:

$$-\Delta S(r) = \frac{\Delta G(r, T + \Delta T) - \Delta G(r, T)}{\Delta T} \qquad (6)$$

PMF calculation using the US method was conducted at 300 K and 320 K and hence, the values of T and ΔT were 300 K and 20 K, respectively. The enthalpic contribution to the free energy, ΔH, can be then calculated using Eq. (7):

$$\Delta H = \Delta G + T \Delta S \qquad (7)$$

In order to elucidate the role of the contribution from the solvent molecules to the PMF, the solvent contribution $\Delta G_w(r)$ to the PMF $\Delta G(r)$ can be evaluated by subtracting the PMF calculated between the particles at 300 K in vacuum $\Delta G_{vac}(r)$, as presented in Eq. (8) thus

$$\Delta G_w(r) = \Delta G(r) - \Delta G_{vac}(r) \qquad (8)$$

4. Results and discussion

4.1. Experimental results

4.1.1. Flux curves

The flux curves of the cross-flow MF experiments are presented in Fig. 4, which shows both the pure water and permeate flux of pristine and fouled PES membranes. After circulating deionized water for 2000 s (33.3 min), the pure water flux of the pristine membrane declined gradually from 2.53×10^4 L m^{-2} h^{-1} to 2.45×10^4 L m^{-2} h^{-1}. This decline in pure water flux may indicate the presence of small amounts of residual foulants from earlier experiments, as was also found by Zhou and Mattsson [37] in a study where the same feed material was used. Immediately after changing the feed from deionized water to MCC suspension, the permeate flux followed a consistent trend with a sharp decline in the flux values observed, showing that the deposition of initial foulants caused a high flow resistance at a constant TMP. The flux values dropped massively to around 500 L m^{-2} h^{-1} (~2% of the initial pure water flux of the pristine membrane) after 3000 s (50 min) of MCC fouling.

Lidén *et al.* [71], who used the same batch of MCC, determined the particle size distribution of mechanically-treated MCC suspensions by laser diffraction. Their results show that virtually all MCC particles are larger than the 0.45 μm nominal pore size of the PES membrane. This suggests that MCC particles are retained on the feed side and the
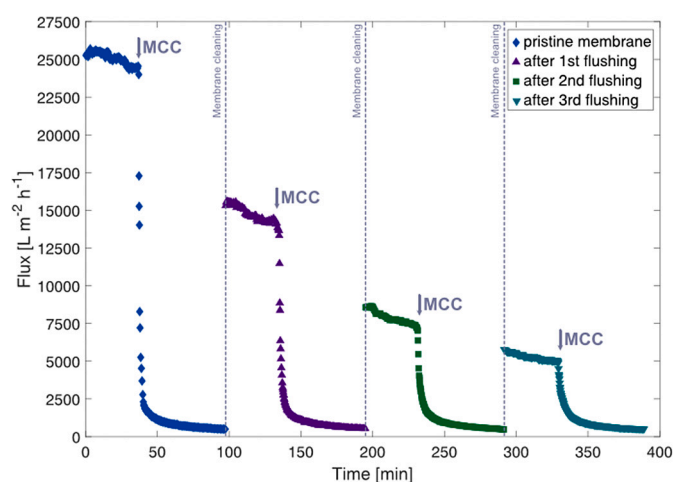

Fig. 4. Flux vs. filtration time for the cross-flow MF sequence of MCC suspensions. Dashed lines indicate membrane cleaning and flushing procedure.

formation of a cake layer is likely the primary fouling mode during the cross-flow MF. However, as the sizes are all nominal, some smaller particles may pass through larger pores and internal pore blocking may therefore still occur to some extent.

Fig. 4 shows that a successive reduction in the pure water flux was observed after each membrane cleaning and flushing procedure despite their thoroughness, as mentioned above and in the Supplementary Material. This demonstrates that an increase in flow resistance after each MF cycle is due to irreversible fouling of the membrane, i.e. MCC particles that are strongly bound to the membrane hinder the flow of liquid. However, despite the large differences in the pure water flux, the behaviour of the permeate flux decline is consistent and appears not to have been influenced by the initial flux. It is worth noting that, since the probe made a small imprint of ~1 mm in diameter (see experimental section), the flux curves were not affected by FDG measurements, as this impact area (~ 1×10^{-6} m^2) was significantly smaller than the active membrane area (2.4×10^{-3} m^2).

4.1.2. FDG profiles

FDG measurements were conducted to determine the properties of the MCC fouling layer during cross-flow MF at 400 mbar TMP. Fig. 5a shows the dp vs. h/d_t profile during cross-flow MF experiments. All FDG measurements were corrected with the $h_{0,\text{offset}}$ value. The filled black circles (•) in Fig. 5a are the results of FDG measurements on a pristine membrane without any fouling layer. This curve followed a consistent
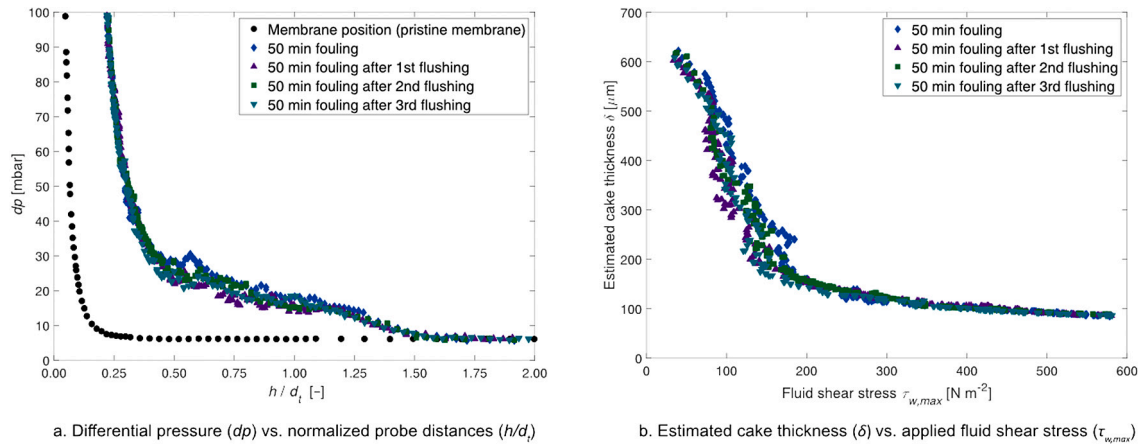
a. Differential pressure (dp) vs. normalized probe distances (h/d_t)

b. Estimated cake thickness (δ) vs. applied fluid shear stress ($\tau_{w,max}$)

Fig. 5. FDG profiles during cross-flow MF of the MCC suspension showing (a) differential pressure, dp, and normalized probe distances, h/d_t, and (b) estimated cake thickness, δ, vs. applied fluid shear, $\tau_{w,max}$, exerted by the FDG probe onto the cake layers formed. N.B. The curves for the membrane position after each cleaning and flushing of the PES membrane were excluded to simplify the data set.

trend with baseline dp values in the asymptotic zone ($h/d_t > 0.25$), while a sharp increase was measured in the incremental zone ($h/d_t \leq 0.25$) as the probe approached the membrane surface.

The difference in h/d_t values during measurements on a pristine membrane without any fouling layer and measurements during MCC fouling represents the thickness of the fouling layers formed, where a larger difference in h/d_t corresponds to a thicker fouling layer. After 3000 s (50 min) of MCC fouling, the initial response resembled that of the pristine membrane up until $h/d_t = 1.50$ but, at $h/d_t < 1.50$, a gradual rise in dp was observed that became much sharper at $h/d_t < 0.50$. In the region $h/d_t = 1.20–1.50$, the increase in flow resistance could be due to concentration polarization or an increase in the viscosity of the suspension resulting from an increased particle concentration just above the fouling layer. In contrast, the increase in flow resistance at $h/d_t < 1.20$ is caused by the formation of a "cake" fouling layer. The non-convergence of the MCC fouling response towards the membrane position measurements at low probe clearing heights demonstrates the resilience of such cake fouling layers formed close to the membrane surface. Measurements made after each cycle of the fouling and cleaning procedure revealed cake fouling layers that are of similar thicknesses: this may indicate that the formation of the cake layer is independent of the increased resistance of the membrane, as supported by the similarity in response despite the large variation in pure water flux after cleaning the membrane.

Fig. 6 presents the membrane and cake resistances, R_m and R_c, respectively, during each cycle of cross-flow MF of MCC suspension. The mean membrane resistance, R_m, increases linearly, from 8.7×10^9 m^{-1} to 3.3×10^{10} m^{-1} during the entire MCC fouling. The gradual increase in R_m after each membrane cleaning and flushing cycle implies the presence of irreversible fouling on the PES membrane that accumulates in each cycle. The cake resistance, R_c, on the other hand, is higher than R_m, but is relatively constant with values ranging from 2.7×10^{11} m^{-1} to 3.1×10^{11} m^{-1}, indicating that the build-up of the cake and its resistance is very similar.

The effect that the applied fluid shear from the gauging fluid flow had on the thickness of the cake layers after each fouling cycle is presented in Fig. 5b. The maximum fluid shear stress was calculated using Eq. (2) and based on the thickness vs. shear stress profile (Fig. 5b), more resilient cake layers were formed closer to the PES membrane and therefore required higher fluid shear to remove them. This trend confirms that the cohesive strength of cake layers formed closer to the membrane is higher than the loose layers formed farther away from it. This difference in cohesive strength is due to the higher local solid pressure exerted on foulants located closer to the membrane surface [34].
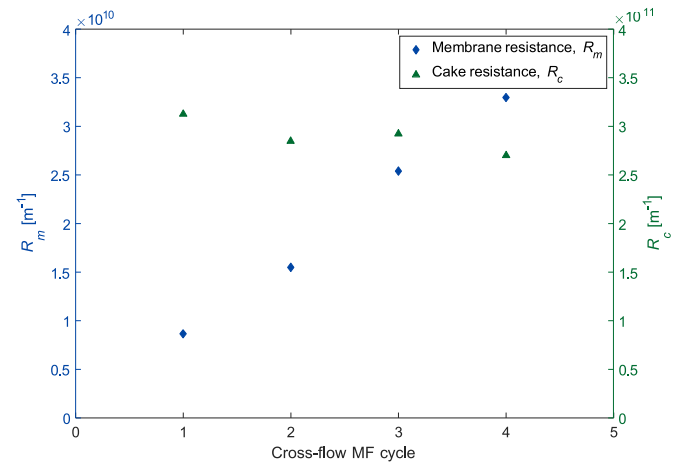

Fig. 6. Membrane and cake resistances during cross-flow MF of MCC suspension. N.B. The membrane resistance is calculated from the average of the resistances before MCC fouling and after cleaning and flushing, except during the 4th cross-flow MF cycle where only the resistance before MCC fouling was considered.

The estimated fouling layer thickness was 616 ± 5 μm for both fouled and re-fouled membranes at an applied shear stress of 37 ± 2 Pa after 3000 s (50 min) of MF (Fig. 5b). As the probe was gradually moved towards the PES membrane, loose cake layers were easily removed. These loose layers were evident in the 35–200 N m^{-2} region of $\tau_{w,max}$, where they were sheared off and became thinner: from an initial cake thickness of ~600 μm down to 150 μm in the remaining layers. More resilient layers were observed when $\tau_{w,max}$ of at least 200 N m^{-2} was applied, with remaining cake thickness values < 150 μm. At low probe clearing heights, thin cake layers with considerably high cohesive strength were formed: it was impossible to remove approximately 85 μm of the cake layers at the maximum applied shear stress of 580 N m^{-2} which, at this remaining cake thickness, corresponds to the diameters of 4–5 nominal/average MCC particles or agglomerates. The gradual increase in the cohesive strength of the cake layers in the direction towards the membrane implies that the particles are most likely closer to each other and become more concentrated in the cake layers closest to the membrane, i.e. the solidosity of the cake layer increases in the direction towards the membrane, and the flow resistance therefore increases in that direction [72].
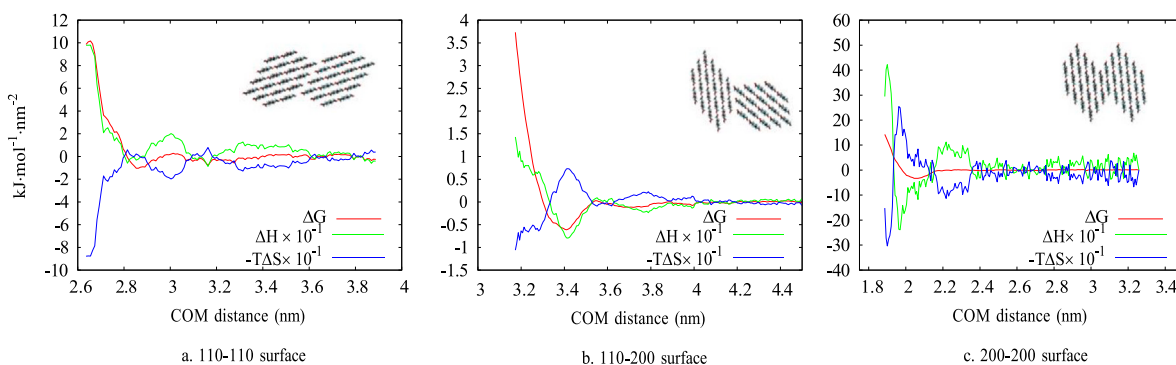
a. 110-110 surface   b. 110-200 surface   c. 200-200 surface

Fig. 7. Cellulose–cellulose interactions, showing the entropic and enthalpic contributions to the free energy during the interaction of different faces of cellulose crystals. ΔH and $-T\Delta S$ are the enthalpic and entropic contributions, respectively, to the free energy, ΔG.

4.2. Simulation results

The nominal pore size of the experimental PES membrane is smaller than virtually all of the MCC particles in the suspension measured by laser diffraction [71]. Furthermore, the experimental results presented above show that some kind of irreversible fouling is formed on the membrane that accumulates in each membrane cleaning cycle. This is a strong indication that particle–membrane interactions occur at the interface, which is of major concern in the present study. It was also observed that the strength of the fouling layer increased in the direction towards the membrane, suggesting that the interaction between particles may be different. In order to shed some light on these phenomena, it is necessary to study the interactions between cellulose particles and PES in water. In the present study, this is done by calculating the potential of mean forces between cellulose–cellulose and cellulose–PES membrane.

4.2.1. Potential of mean force

It is important that interactions involving all faces of a cellulose crystal are considered in order to study the particle–particle interaction involved in the systems investigated in this work. As mentioned previously, cellulose crystals have two different types of surfaces, namely 110 and 200, so interactions between the 110–110, 110–200 and 200–200 planes are examined [64]. The PMF profiles of these planes, normalized by the area of the interacting surfaces, are presented in Fig. 7. In order to facilitate a better visual comparison among the PMF profiles from different cases while not losing the graphic resolution of the individual graphs, the enthalpic and the entropic contributions are scaled by a factor of 10^{-1}, while the values of the free energy are not scaled. Similarly, the axes has been adjusted to emphasize the contribution of respective curves.

The repulsive cellulose–cellulose interactions increase significantly when the interacting surfaces become closer. However, a deep attractive primary minimum is observed in all cases that decrease in the order: 200–200, 110–110 and 110–200. The presence of an attractive region near the crystal interfaces suggests that the cellulose crystals have a tendency to bind firmly to each other when they approach closer under the influence of external forces, and that redispersion seems relatively difficult. The gradual increase of the local solid pressure towards the surface of the PES membrane [34] during the cross-flow MF exerts a high external pressure force on cellulose particles. This, in turn, pushes the cellulose particles towards each other, eventually entering the primary minimum, given that the pressure forces are sufficiently large to overcome the primary maximum. Hence, closer to the restrained interfaces [73], such as the PES membrane in this study, where there is a high local solid pressure, the cellulose crystals may enter into the attractive region described by the primary minimum and are strongly bound to each other and thereby form a compact cake layer, as observed during the MF experiments described above.

Similarly, the PMF profiles for cellulose–PES interactions are shown in Fig. 8. Cellulose–PES interactions are more repulsive than cellulose–cellulose interactions, suggesting that cellulose crystals have a lesser tendency to approach the PES surface. The interparticle distance where the attractive and repulsive forces are in balance as predicted by the primary energy minima does, however, exist at low COM distances, similar to the cases of the cellulose–cellulose interactions. The existence of these lower energy regions suggests that the cellulose crystals tend to remain in the area closer to the PES membrane as they are driven towards the PES–water interface by external forces during cross-flow filtration. This may give rise to the so-called "skin formation" near the PES surface, as discussed in previous studies [71,74]. It is interesting to note that all faces of cellulose nanocrystals show attraction to the PES membrane, which has a partial hydrophobic character [75]; its water contact angle is approximately 67°.

4.2.2. Entropic and enthalpic contributions to the free energy profile

The entropic contribution, $-T\Delta S$, and the enthalpic contribution, ΔH, to the PMF, ΔG, at 300 K is obtained through Eqs. (6) and (7) and are shown in Fig. 7 and Fig. 8, respectively. The entropic and enthalpic contributions act in opposite directions and their relative proportions depend on the interparticle distances involved. It is observed that the stabilizing effect of these contributions depends upon the interacting face of the cellulose crystals. For instance, the interaction between 110–110 faces, as shown in Fig. 7a, demonstrates that an energy barrier exists between COM separation distances of 2.9 and 3.1 nm. Although the entropic contribution, $-T\Delta S$, suggests an increase in entropy which might be due to the expulsion of interfacial water molecules when two cellulose surfaces come closer, the process nevertheless becomes unfavourable due to the unfavourable enthalpic contribution. At the contact minimum, the entropy seems to decrease along with the enthalpic contribution, which might be due to the higher structuring of water molecules at the interface as the particles become closer. Beyond the contact minimum, as the particles are pushed further towards each other, the unfavourable enthalpic contribution controls the higher repulsion that occurs between the particles, thereby making it impossible for the particles to get any closer.

A similar trend is observed during the interaction of the 200–200 surfaces, as shown in Fig. 7c. It seems that when similar surfaces interact, the hydration repulsion caused by a water molecule, which depends on its orientation relative to the surface normal, plays an important role in the aggregation process of cellulose crystals. The interaction of similar surfaces implies a higher probability of exposure of similar groups of the solvent molecules towards each interacting surface: this might be the cause of the similar tendency of the entropic and enthalpic contributions to the free energy profile during the interaction of 110–110 and 200–200 surfaces. However, there exists a secondary minimum during the interaction of 110–200 surfaces, as shown in Fig. 7b, followed by a primary minimum as the particles come closer. The solvent
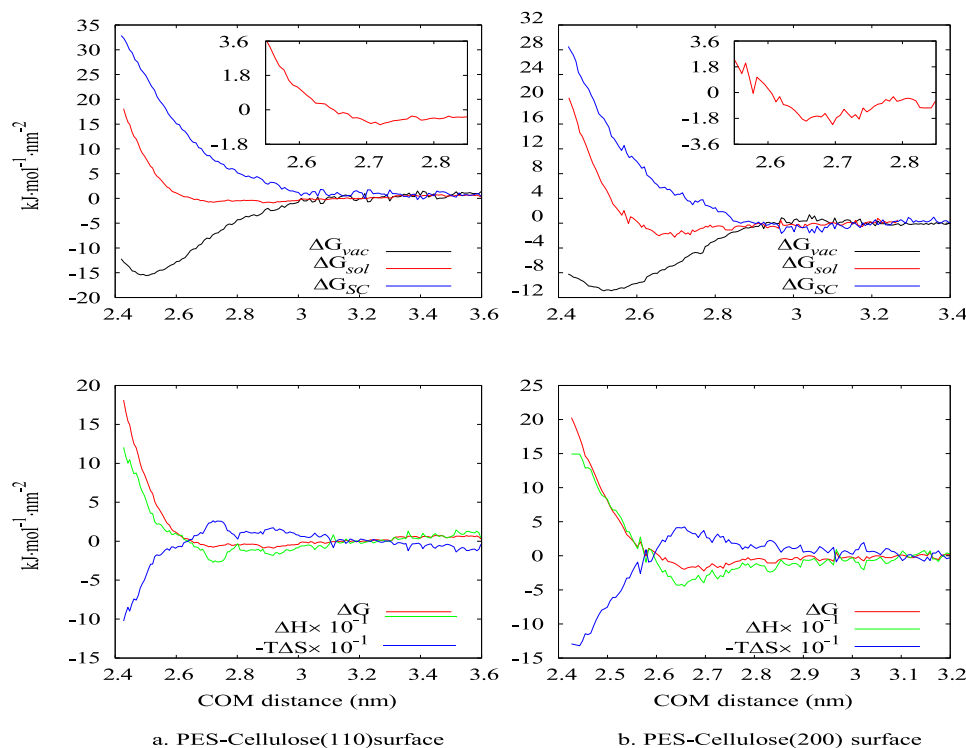
Fig. 8. PES–cellulose interactions, showing the free energy profile along with the associated entropic and enthalpic contributions for the interaction of the membrane surface and the different faces of cellulose crystals. ΔH and $-T\Delta S$ are the enthalpic and entropic contributions to the free energy, ΔG, respectively. Similarly, ΔG_{vac} and $\Delta G_{sol}(=\Delta G)$ are the free energy profiles between the cellulose and PES surface in vacuum and water, respectively, and ΔG_{SC} represents the solvent contribution to the free energy profile in water.

molecules appear to be highly organized, as reflected by a decrease in entropy in this region: the greater structuring of water molecules could prevent the association of 110–200 surfaces. This implies that the hydration layer around the cellulose particles plays a significant role in the fouling process of the PES membrane, which is in agreement with the observations by Miao *et al.* [76] in their work on the effect of ion hydration on the membrane fouling by proteins. Similarly, Xu *et al.* [77] reported the effect of hydrophobic interactions and hydrogen bonds in an interesting review of the roles of membrane-foulant and foulant–foulant interactions in organic fouling. Nevertheless, it should be noted that the overall free energy of association is the least for 110–200 surfaces, in which the agglomeration of these two surfaces is less probable than in other cases. A similar trend of free energy profiles was also observed by Garg *et al.* [78]. Furthermore, the results in the present study reveal that the contribution of water molecules plays a significant role in the free energy profiles of the cellulose–PES interactions, suggesting that hydration or water network affects the PES fouling with cellulose.

In cross-flow filtration processes, the TMP acts as the driving force for filtration and is applied perpendicular to the membrane. This pressure drives the dispersed particles from the bulk fluid towards the membrane, although some interfacial particles may interact with the membrane in the absence of pressure. However, the application of pressure affects the interaction of interfacial particles with the membrane to a greater extent, hence forming a pronounced fouling layer.

The free energy profiles of 110-PES and 200-PES surfaces are shown in Fig. 8. The profile of the interaction of the cellulose (110) surface with the PES membrane indicates that the entropy of the system decreases: it is unfavourable until the contact minimum is reached at the COM distance between 2.65–2.77 nm, with enthalpy being favourable at that condition. Once the contact minimum is passed, the entropy increases drastically and is favourable for the adsorption of the 110 surface onto the PES surface. The unfavourable enthalpic contribution dominates the region after the contact minimum resulting in high repulsion between the cellulose (110) surface and the PES membrane.

The free energy profile of the interaction of the cellulose (200) surface with the PES membrane shows a similar scenario. At the contact minimum, the system is stabilized by the enthalpic contribution. It can therefore be concluded that, under the effect of external pressure forces, the cellulose particles approach the PES membrane and tend to remain in the region of the first energy minimum, which results in the membrane being fouled. Our earlier analysis has shown that there is a lower probability that a cellulose (110) surface is adsorbed onto a cellulose (200) surface, which indicates that a larger quantity of cellulose(100) and cellulose(200) surfaces exists freely in the cellulose–water suspension. Nevertheless, the contact minimum for the case when PES surface interacts with the cellulose (200) surface is lower than the cellulose (100) surface, suggesting that the cellulose (200) surface binds more readily with the PES membrane than the cellulose (100) surface. Consequently, the interaction of the PES–cellulose (200) surface should play a more important role in the filtration process. Fig. 8 suggests that the interaction of particles at the contact minimum, which defines the stable state of a system, is exothermic. It can thereby be inferred that an increase in the temperature of the system will negatively affect the existence of cellulose crystals at the first energy minimum. It indicates that an increase in the temperature of the suspension and a decrease in the entropy via lowering the Reynolds number could lead to a lower strength of the fouling layer; this effect was reported experimentally by Zhou and Mattsson [37]. A similar trend for the different contributions to the free energy was also observed in the cellulose 110–110 interacting surfaces.

The contribution made by the solvent molecules to the free energy profiles of the interacting particles was also analysed. A negative effect on the overall free energy profile near the interface was observed in all cases, as shown in Fig. S4; this negative contribution of the solvent is due to hydration of the interacting particles and has been studied well [79,80]. It has been suggested that the solvent contribution leading to the hydration repulsion phenomenon involves the overlapping of interfacial layers: the orientation of the solvent layers near the interface may therefore play an important role in this process. In most of the

cases in the present study, the repulsion observed was found to be driven by enthalpy at very short separations, which is in line with the "water structure" concept of hydration theory [81,82]. In this model, the repulsion at the interface is caused by interactions imposed by the structure of the solvent, which implies that the mechanism is basically of energetic origin. It should be expected that the enthalpic contribution dominates the free energy, which is also observed in the present study. Therefore, the steep repulsive interaction observed after the primary contact minimum towards the PES surface should be the result of highly organized water molecules adsorbed onto the PES surface.

5. Concluding remarks

This work has investigated the fouling behaviour of a dilute MCC suspension through experimental cross-flow MF and MD simulations. FDG measurements were conducted to estimate the thickness and cohesive strength of the cake layers formed, while MD simulations were carried out to determine the influence of the cellulose–cellulose and cellulose–PES interactions on the free energy profile.

FDG measurements revealed the formation of resilient cake layers of considerably high strength close to the PES membrane surface. This could be explained by the primary energy minima estimated through MD simulations, where the attractive and repulsive forces between the cellulose particles as well as the cellulose particles and the PES membrane are in balance. For the cellulose–cellulose interactions, the migration of cellulose particles towards the region of minimum energy under the influence of high local solid pressure [34] explains the formation of resilient cellulose cake layers.

The free energy profiles showed that the stabilizing effect of these contributions depends on the interacting face of the cellulose crystals. Interfacial adsorption seemed to be unfavoured by the positive entropic change and favoured by the enthalpic contribution of cellulose crystals with the PES membrane at the contact minimum. These results indicate that the fouling of the PES membrane via adsorption of cellulose particles onto the PES surface is an exothermic process. Therefore, a controlled increase in the temperature of the suspension and the generation of less entropy by lowering the Reynolds number [37] could aid in reducing the strength of the fouling layer.

Nomenclature

Roman

d	Inner diameter of the gauge tube [m]
dp	Pressure drop over the FDG probe [mbar]
d_t	Inner diameter of the nozzle orifice [m]
h	Gauge height above the fouling layer [m]
h_0	Gauge height above the membrane [m]
J	Flux [L m^{-2} h^{-1}]
m_g	Gauging mass flow rate [kg s^{-1}]
r	Interparticle separation [m]
R_c	Cake resistance [m^{-1}]
R_m	Membrane resistance [m^{-1}]
R_T	Total resistance [m^{-1}]
Re_{duct}	Duct flow Reynolds number [–]

Greek

ΔG	Free energy [J mol^{-1} m^{-2}]
ΔH	Enthalpic contribution to the free energy [J mol^{-1} m^{-2}]
δ	Fouling layer thickness [m]
μ	Dynamic viscosity of the fluid [Pa s]
Π	Osmotic pressure [Pa]
ρ	Density of the fluid [kg m^{-3}]

$\tau_{w,max}$	Fluid shear stress [Pa]
$T \Delta S$	Entropic contribution to the free energy [J mol^{-1} m^{-2}]

Acronyms

CNC	Cellulose nanocrystal
COM	Center of mass
CFV	Cross-flow velocity [m s^{-1}]
FDG	Fluid dynamic gauging
MD	Molecular dynamics
MF	Microfiltration
MCC	Microcrystalline cellulose
OPLS-AA	All-atom optimized potentials for liquid simulations
PES	Polyethersulfone
PMF	Potential of mean force
SEM	Scanning electron microscopy
SPC/E	Extended simple point-charge
SPME	Smooth Particle Mesh Ewald
TMP	Transmembrane pressure [mbar]
US	Umbrella sampling
WHAM	Weighted histogram analysis method

Declaration of competing interest

The authors declare that they have no known competing financial interests or personal relationships that could have appeared to influence the work reported in this paper.

Data availability

Data will be made available on request.

Appendix A. Supplementary data

Supplementary material related to this article can be found online at https://doi.org/10.1016/j.memsci.2022.121272.

References

[1] C. Abels, F. Carstensen, M. Wessling, Membrane processes in biorefinery applications, J. Membr. Sci. 444 (2013) 285–317, http://dx.doi.org/10.1016/j.memsci.2013.05.030.

[2] N. Hajilary, M. Rezakazemi, S. Shirazian, Biofuel types and membrane separation, Environ. Chem. Lett. 17 (2019) 1–18, http://dx.doi.org/10.1007/s10311-018-0777-9.

[3] H.-J. Huang, S. Ramaswamy, U.W. Tschirner, B.V. Ramarao, A review of separation technologies in current and future biorefineries, Sep. Purif. Technol. 62 (2008) 1–21, http://dx.doi.org/10.1016/j.seppur.2007.12.011.

[4] F. Lipnizki, J. Thuvander, G. Rudolph, Membrane processes and applications for biorefineries, Curr. Trends Future Dev. (Bio-) Membr. (2019) 283–301, http://dx.doi.org/10.1016/j.memsci.2013.05.030.

[5] Y. He, D.M. Bagley, K.T. Leung, S.N. Liss, B.-Q. Liao, Recent advances in membrane technologies for biorefining and bioenergy production, J. Biotech. Adv. 30 (2012) 817–858, http://dx.doi.org/10.1016/j.biotechadv.2012.01.015.

[6] M. Kamali, Z. Khodaparast, Review on recent developments on pulp and paper mill wastewater treatment, J. Ecol. Environ. 114 (2015) 326–342, http://dx.doi.org/10.1016/j.ecoenv.2014.05.005.

[7] L.T. Yogarathinam, A.F. Ismail, P.S. Goh, A. Gangasalam, Challenges of membrane technology in biorefineries, J. Appl. Membr. Sci. Technol. 24 (2020) 75–82, http://dx.doi.org/10.11113/amst.v24n3.197.

[8] W.J. Koros, Y.H. Ma, T. Shimidzu, Terminology for membranes and membrane processes (IUPAC recommendation 1996), J. Membr. Sci. 120 (1996) 149–159, http://dx.doi.org/10.1016/0376-7388(96)82861-4.

[9] M. Mulder, Basic Principles of Membrane Technology, 1996, http://dx.doi.org/10.1007/978-94-009-1766-8.

[10] V. Chen, H. Li, A.G. Fane, Non-invasive observation of synthetic membrane processes — A review of methods, J. Membr. Sci. 241 (2004) 23–44, http://dx.doi.org/10.1016/j.memsci.2004.04.029.

[11] G. Rudolph, T. Virtanen, M. Ferrando, C. Güell, F. Lipnizki, M. Kallioinen, A review of in situ real-time monitoring techniques for membrane fouling in the biotechnology, biorefinery and food sectors, J. Membr. Sci. 588 (2019) 117221, http://dx.doi.org/10.1016/j.memsci.2019.117221.

[12] R. Chan, V. Chen, Characterization of protein fouling on membranes: Opportunities and challenges, J. Membr. Sci. 242 (2004) 169–188, http://dx.doi.org/10.1016/j.memsci.2004.01.029.

[13] W.J. Lau, A. Ismail, P.S. Goh, N. Hilal, B.S. Ooi, Characterization methods of thin film composite nanofiltration membranes, Sep. Purif. Rev. 44 (2015) 135–156, http://dx.doi.org/10.1080/15422119.2014.882355.

[14] S. Mikhaylin, L. Bazinet, Fouling on ion-exchange membranes: Classification, characterization and strategies of prevention and control, Adv. Colloid Interf. Sci. 229 (2016) 34–56, http://dx.doi.org/10.1016/j.cis.2015.12.006.

[15] R.W. Field, D. Wu, J.A. Howell, B.B. Gupta, Critical flux concept for microfiltration fouling, J. Membr. Sci. 100 (1995) 259–272, http://dx.doi.org/10.1016/0376-7388(94)00265-Z.

[16] E. Eckstein, D. Bailey, A. Shapiro, Self-diffusion of particles in shear flow of a suspension, J. Fluid Mech. 79 (1977) 191–208, http://dx.doi.org/10.1017/S0022112077000111.

[17] F.W. Altena, G. Belfort, Lateral migration of spherical particles in porous flow channels: Application to membrane filtration, Chem. Eng. Sci. 39 (1984) 343–355, http://dx.doi.org/10.1016/0009-2509(84)80033-0.

[18] A. Broeckmann, J. Busch, T. Wintgens, W. Marquardt, Modeling of pore blocking and cake layer formation in membrane filtration for wastewater treatment, Desalination 189 (2006) 97–109, http://dx.doi.org/10.1016/j.desal.2005.06.018.

[19] Y. Marselina, P. Le-Clech, R. Stuetz, V. Chen, Detailed characterisation of fouling deposition and removal on a hollow fibre membrane by direct observation technique, Desalination 231 (2008) 3–11, http://dx.doi.org/10.1016/j.desal.2007.11.033.

[20] T. Schluep, F. Widmer, Initial transient effects during cross flow microfiltration of yeast suspensions, J. Membr. Sci. 115 (1996) 133–145, http://dx.doi.org/10.1016/0376-7388(95)00321-5.

[21] A.P. Mairal, A.R. Greenberg, W.B. Krantz, L.J. Bond, Real-time measurement of inorganic fouling of RO desalination membranes using ultrasonic time-domain reflectometry, J. Membr. Sci. 159 (1999) 185–196, http://dx.doi.org/10.1016/S0376-7388(99)00058-7.

[22] S. Yao, M. Costello, A.G. Fane, J.M. Pope, Non-invasive observation of flow profiles and polarisation layers in hollow fibre membrane filtration modules using NMR micro-imaging, J. Membr. Sci. 99 (1995) 207–216, http://dx.doi.org/10.1016/0376-7388(94)00219-O.

[23] J. Kromkamp, F. Faber, K. Schroen, R. Boom, Effects of particle size segregation on crossflow microfiltration performance: control mechanism for concentration polarisation and particle fractionation, J. Membr. Sci. 268 (2006) 189–197, http://dx.doi.org/10.1016/j.memsci.2005.06.012.

[24] C. David, F. Pignon, T. Narayanan, M. Sztucki, G. Gésan-Guiziou, A. Magnin, Spatial and temporal in situ evolution of the concentration profile during casein micelle ultrafiltration probed by small-angle x-ray scattering, Langmuir 24 (2008) 4523–4529, http://dx.doi.org/10.1021/la703256s.

[25] H.G.L. Coster, T.C. Chilcott, A.C.F. Coster, Impedance spectroscopy of interfaces, membranes and ultrastructures, Bioelectrochem. Bioenerg. 40 (1996) 79–98, http://dx.doi.org/10.1016/0302-4598(96)05064-7.

[26] T.R. Tuladhar, W.R. Paterson, N. Macleod, D.I. Wilson, Development of a novel non-contact proximity gauge for thickness measurement of soft deposits and its application in fouling studies, Can. J. Chem. Eng. 78 (2000) 935–947, http://dx.doi.org/10.1002/cjce.5450780511.

[27] T.R. Tuladhar, W.R. Paterson, D.I. Wilson, Dynamic gauging in duct flows, Can. J. Chem. Eng. 81 (2008) 279–284, http://dx.doi.org/10.1002/cjce.5450810214.

[28] Y.M.J. Chew, W.R. Paterson, D.I. Wilson, Fluid dynamic gauging: A new tool to study deposition on porous surfaces, J. Membr. Sci. 296 (2007) 29–41, http://dx.doi.org/10.1016/j.memsci.2007.03.009.

[29] S.A. Jones, Y.M.J. Chew, M.R. Bird, D.I. Wilson, The application of fluid dynamic gauging in the investigation of synthetic membrane fouling phenomena, Food Bioprod. Process. 88 (2010) 409–418, http://dx.doi.org/10.1016/j.fbp.2010.07.004.

[30] V.Y. Lister, C. Lucas, P.W. Gordon, Y.M.J. Chew, D.I. Wilson, Pressure mode fluid dynamic gauging for studying cake build-up in cross-flow microfiltration, J. Membr. Sci. 366 (2011) 304–313, http://dx.doi.org/10.1016/j.memsci.2010.10.017.

[31] W.J.T. Lewis, Y.M.J. Chew, M.R. Bird, The application of fluid dynamic gauging in characterising cake deposition during the cross-flow microfiltration of a yeast suspension, J. Membr. Sci. 405–406 (2012) 113–122, http://dx.doi.org/10.1016/j.memsci.2012.02.065.

[32] M.K. Jørgensen, T. Mattsson, Quantifying charge effects on fouling layer strength and (ir)removability during cross-flow microfiltration, Membranes 11 (2021) 28, http://dx.doi.org/10.3390/membranes11010028.

[33] T. Mattsson, W.J.T. Lewis, Y.M.J. Chew, M.R. Bird, In situ investigation of soft cake fouling layers using fluid dynamic gauging, Food Bioprod. Process. 93 (2015) 205–210, http://dx.doi.org/10.1016/j.fbp.2014.09.003.

[34] T. Mattsson, W.J.T. Lewis, Y.M.J. Chew, M.R. Bird, The use of fluid dynamic gauging in investigating the thickness and cohesive strength of cake fouling layers formed during cross-flow microfiltration, Sep. Purif. Technol. 198 (2018) 25–30, http://dx.doi.org/10.1016/j.seppur.2017.01.040.

[35] W.J.T. Lewis, T. Mattsson, Y.M.J. Chew, M.R. Bird, Investigation of cake fouling and pore blocking phenomena using fluid dynamic gauging and critical flux models, J. Membr. Sci. 533 (2017) 38–47, http://dx.doi.org/10.1016/j.memsci.2017.03.020.

[36] M. Zhou, H. Sandström, M.P. Belioka, T. Pettersson, T. Mattsson, Investigation of the cohesive strength of membrane fouling layers formed during cross-flow microfiltration: The effects of pH adjustment on the properties and fouling characteristics of microcrystalline cellulose, Chem. Eng. Res. Des. 149 (2019) 52–64, http://dx.doi.org/10.1016/j.cherd.2019.06.037.

[37] M. Zhou, T. Mattsson, Effect of crossflow regime on the deposit and cohesive strength of membrane surface fouling layers, Food Bioprod. Process. 115 (2019) 185–193, http://dx.doi.org/10.1016/j.fbp.2019.03.013.

[38] M.B. Tanis-Kanbur, S. Halitoğlu-Velioğlu, H.J. Tanudjaja, X. Hu, J.W. Chew, Understanding membrane fouling by oil-in-water emulsion via experiments and molecular dynamics simulations, J. Membr. Sci. 566 (2018) 140–150, http://dx.doi.org/10.1016/j.memsci.2018.08.067.

[39] G.M. Meconi, N. Ballard, J.M. Asua, R. Zangi, Adsorption and desorption behavior of ionic and nonionic surfactants on polymer surfaces, Soft Matter 12 (2016) 9692–9704, http://dx.doi.org/10.1039/C6SM01878E.

[40] Q. Shi, Y. Su, W. Chen, J. Peng, L. Nie, L. Zhang, Z. Jiang, Grafting short-chain amino acids onto membrane surfaces to resist protein fouling, J. Membr. Sci. 366 (2011) 98–404, http://dx.doi.org/10.1016/j.memsci.2010.10.032.

[41] Y. Ma, A.L. Zydney, J.W. Chew, Membrane fouling by lysozyme: Effect of local interaction, AIChE J. 67 (2021) http://dx.doi.org/10.1002/aic.17212.

[42] Y. Ma, S. Velioğlu, Z. Yin, R. Wang, J.W. Chew, Molecular dynamics investigation of membrane fouling in organic solvents, J. Membr. Sci. 632 (2021) 119329, http://dx.doi.org/10.1016/j.memsci.2021.119329.

[43] Z.-Y. Liu, Q. Jiang, Z. Jin, Z. Sun, W. Ma, Y. Wang, Understanding the antifouling mechanism of zwitterionic monomer grafted PVDF membranes: A comparative experimental and molecular dynamics simulation study, ACS Appl. Mater. Interfaces 11 (2019) 14408–14417, http://dx.doi.org/10.1021/acsami.8b22059.

[44] S.-W. Hung, P.-Y. Hsiao, M.-C. Lu, C.-C. Chieng, Thermodynamic investigations using molecular dynamics simulations with potential of mean force calculations for cardiotoxin protein adsorption on mixed self-assembled monolayers, J. Phys. Chem. B 116 (2012) 12661–12668, http://dx.doi.org/10.1021/jp304695w.

[45] K. Arandia, U. Balyan, T. Mattsson, Development of a fluid dynamic gauging method for the characterization of fouling behavior during cross-flow filtration of a wood extraction liquor, Food Bioprod. Process. 128 (2021) 30–40, http://dx.doi.org/10.1016/j.fbp.2021.04.009.

[46] W.J.T. Lewis, Advanced Studies of Membrane Fouling: Investigation of Cake Fouling using Fluid Dynamic Gauging, University of Bath, 2015, https://researchportal.bath.ac.uk/en/studentTheses/advanced-studies-of-membrane-fouling.

[47] J. Wetterling, T. Mattsson, H. Theliander, Effects of surface structure on the filtration properties of microcrystalline cellulose, Sep. Purif. Technol. 136 (2014) 1–9, http://dx.doi.org/10.1016/j.seppur.2014.08.031.

[48] M.J. Abraham, T. Murtola, R. Schulz, S. Páll, J.C. Smith, B. Hess, E. Lindahl, GROMACS: High performance molecular simulations through multi-level parallelism from laptops to supercomputers, SoftwareX 1–2 (2015) 19–25, http://dx.doi.org/10.1016/j.softx.2015.06.001.

[49] M. Bergenstråhle, J. Wohlert, M.E. Himmel, J.W. Brady, Simulation studies of the insolubility of cellulose, Carbohydr. Res. 345 (2010) 2060–2066, http://dx.doi.org/10.1016/j.carres.2010.06.017.

[50] E.L. Lindh, M. Bergenstråhle-Wohlert, C. Terenzi, L. Salmén, I. Furó, Non-exchanging hydroxyl groups on the surface of cellulose fibrils: The role of interaction with water, Carbohydr. Res. 434 (2016) 136–142, http://dx.doi.org/10.1016/j.carres.2016.09.006.

[51] J.A. Lemkul, D.R. Bevan, Assessing the stability of Alzheimer's amyloid protofibrils using molecular dynamics, J. Phys. Chem. B 114 (2010) 1652–1660, http://dx.doi.org/10.1021/jp9110794.

[52] M.S.J. Sajib, Y. Wei, A. Mishra, L. Zhang, K.-I. Nomura, R.K. Kalia, P. Vashishta, A. Nakano, S. Murad, T. Wei, Atomistic simulations of biofouling and molecular transfer of a cross-linked aromatic polyamide membrane for desalination, Langmuir 36 (2020) 7658–7668, http://dx.doi.org/10.1021/acs.langmuir.0c01308.

[53] K. Li, L. Liu, H. Wu, S. Li, C. Yu, Y. Zhou, W. Huanga, D. Yan, Understanding the temperature effect on transport dynamics and structures in polyamide reverse osmosis system via molecular dynamics simulations, Phys. Chem. Chem. Phys. 20 (2018) 29996–30005, http://dx.doi.org/10.1039/c8cp05825c.

[54] U. Essmann, L. Perera, M.L. Berkowitz, T. Darden, H. Lee, L.G. Pedersen, A smooth particle mesh Ewald method, J. Chem. Phys. 103 (1995) 8577–8593, http://dx.doi.org/10.1063/1.470117.

[55] G. Bussi, D. Donadio, M. Parrinello, Canonical sampling through velocity rescaling, J. Chem. Phys. 126 (2007) 014101, http://dx.doi.org/10.1063/1.2408420.

[56] H.J.C. Berendsen, J.R. Grigera, T.P. Straatsma, The missing term in effective pair potentials, J. Chem. Phys. 91 (1987) 6269–6271, http://dx.doi.org/10.1021/j100308a038.

[57] S. Miyamoto, P.A. Kollman, Settle: An analytical version of the SHAKE and RATTLE algorithm for rigid water models, J. Comput. Chem. 13 (1992) 952–962, http://dx.doi.org/10.1002/jcc.540130805.

[58] W.L. Jorgensen, D.S. Maxwell, J. Tirado-Rives, Development and testing of the OPLS all-atom force field on conformational energetics and properties of organic liquids, J. Am. Chem. Soc. 118 (1996) 11225–11236, http://dx.doi.org/10.1021/ja9621760.

[59] A. Paajanen, Y. Sonavane, D. Ignasiak, J.A. Ketoja, T. Maloney, S. Paavilainen, Atomistic molecular dynamics simulations on the interaction of TEMPO-oxidized cellulose nanofibrils in water, Cellulose 23 (2016) 3449–3462, http://dx.doi.org/10.1007/s10570-016-1076-x.

[60] A. Paajanen, S. Ceccherini, T. Maloney, J.A. Ketoja, Chirality and bound water in the hierarchical cellulose structure, Cellulose 26 (2019) 5877–5892, http://dx.doi.org/10.1007/s10570-019-02525-7.

[61] B.P. Roberts, G.Y. Krippner, M.J. Scanlon, D.K. Chalmers, Molecular dynamics of variegated polyamide dendrimers, Macromolecules 42 (2009) 2784–2794, http://dx.doi.org/10.1021/ma8021579.

[62] S. Bisoi, A.K. Mandal, V. Padmanabhan, S. Banerjee, Aromatic polyamides containing trityl substituted triphenylamine: Gas transport properties and molecular dynamics simulations, J. Membr. Sci. 522 (2017) 77–90, http://dx.doi.org/10.1016/j.memsci.2016.09.007.

[63] Y. Nishiyama, P. Langan, H. Chanzy, Crystal structure and hydrogen-bonding system in cellulose $I\beta$ from synchrotron x-ray and neutron fiber diffraction, J. Am. Chem. Soc. 124 (2002) 9074–9082, http://dx.doi.org/10.1021/ja0257319.

[64] A.Y. Mehandzhiyski, N. Rolland, M. Garg, J. Wohlert, M. Linares, I. Zozoulenko, A novel supra coarse-grained model for cellulose, Cellulose 27 (2020) 4221–4234, http://dx.doi.org/10.1007/s10570-020-03068-y.

[65] M.D. Hanwell, D.E. Curtis, D.C. Lonie, T. Vandermeersch, E. Zurek, G.R. Hutchison, Avogadro: an advanced semantic chemical editor, visualization, and analysis platform, J. Cheminform. 4 (2012) 17, http://dx.doi.org/10.1186/1758-2946-4-17.

[66] W.-Y. Ahn, A.G. Kalinichev, M.M. Clark, Effects of background cations on the fouling of polyethersulfone membranes by natural organic matter: Experimental and molecular modeling study, J. Membr. Sci. 309 (2008) 128–140, http://dx.doi.org/10.1016/j.memsci.2007.10.023.

[67] T.F. Shi, J. Wei, L.J. An, B.Y. Li, Molecular dynamics simulation of sub-transition for polyethersulfone, Macromol. Theory Simul. 10 (2001) 232–236, http://dx.doi.org/10.1002/1521-3919(20010401)10:4<232::AID-MATS232>3.0.CO;2-E.

[68] C. Barth, B.A. Wolf, Quick and reliable routes to phase diagrams for polyethersulfone and polysulfone membrane formation, Macromol. Chem. Phys. 201 (2000) 365–374, http://dx.doi.org/10.1002/(SICI)1521-3935(20000201)201:3<365::AID-MACP365>3.0.CO;2-5.

[69] S. Kumar, J.M. Rosenberg, D. Bouzida, R.H. Swendsen, P.A. Kollman, Multidimensional free-energy calculations using the weighted histogram analysis method, J. Comput. Chem. 16 (1995) 1339–1350, http://dx.doi.org/10.1002/jcc.540161104.

[70] N. Choudhury, B.M. Pettitt, Enthalpy-entropy contributions to the potential of mean force of nanoscopic hydrophobic solutes, J. Phys. Chem. B 110 (2006) 8459–8463, http://dx.doi.org/10.1021/jp056909r.

[71] A. Lidén, N.K. Karna, T. Mattsson, H. Theliander, Dewatering microcrystalline cellulose: The influence of ionic strength, Sep. Purif. Technol. 264 (2021) 118245, http://dx.doi.org/10.1016/j.seppur.2020.118245.

[72] R. Wakeman, The influence of particle properties on filtration, Sep. Purif. Technol. 58 (2007) 234–241, http://dx.doi.org/10.1016/j.seppur.2007.03.018.

[73] S. Saha, U.D. Hemraz, Y. Boluk, The effects of high pressure and high temperature in semidilute aqueous cellulose nanocrystal suspensions, Biomacromolecules 21 (2020) 1031–1035, http://dx.doi.org/10.1021/acs.biomac.9b01130.

[74] T. Mattsson, M. Sedin, H. Theliander, On the local filtration properties of microcrystalline cellulose during dead-end filtration, Chem. Eng. Sci. 72 (2012) 51–60, http://dx.doi.org/10.1016/j.ces.2012.01.022.

[75] W. Fu, C. Carbrello, X. Wu, W. Zhang, Visualizing and quantifying the nanoscale hydrophobicity and chemical distribution of surface modified polyethersulfone (PES) membranes, Nanoscale 9 (2017) 15550–15557, http://dx.doi.org/10.1039/C7NR03772D.

[76] R. Miao, L. Wang, M. Zhu, D. Deng, S. Li, J. Wang, T. Liu, Y. Lv, Effect of hydration forces on protein fouling of ultrafiltration membranes: The role of protein charge, hydrated ion species, and membrane hydrophilicity, Environ. Sci. Technol. 51 (2016) 167–174, http://dx.doi.org/10.1021/acs.est.6b03660.

[77] H. Xu, K. Xiao, X. Wang, S. Liang, C. Wei, X. Wen, X. Huang, Outlining the roles of membrane-foulant and foulant-foulant interactions in organic fouling during microfiltration and ultrafiltration: A mini-review, Front. Chem. 8 (2020) 417, http://dx.doi.org/10.3389/fchem.2020.00417.

[78] M. Garg, M. Linares, I. Zozoulenko, Theoretical rationalization of self-assembly of cellulose nanocrystals: Effect of surface modifications and counterions, Biomacromolecules 21 (2020) 3069–3080, http://dx.doi.org/10.1021/acs.biomac.0c00469.

[79] E. Sobolewski, M. Makowski, C. Czaplewski, A. Liwo, S. Ołdziej, H.A. Scheraga, Potential of mean force of hydrophobic association: Dependence on solute size, J. Phys. Chem. B 111 (2007) 10765–10774, http://dx.doi.org/10.1021/jp070594t.

[80] S. Ou, S. Patel, B.A. Bauer, Free energetics of carbon nanotube association in pure and aqueous ionic solutions, J. Phys. Chem. B 116 (2012) 8154–8168, http://dx.doi.org/10.1021/jp3025717.

[81] S. Marčelja, N. Radić, Repulsion of interfaces due to boundary water, Chem. Phys. Lett. 42 (1976) 129–130, http://dx.doi.org/10.1016/0009-2614(76)80567-2.

[82] D.W.R. Gruen, S. Marčelja, Spatially varying polarization in water, a model for the electric double layer and the hydration force, J. Chem. Soc. Faraday Trans. 2 (79) (1983) 225–242, http://dx.doi.org/10.1039/F29837900225.